

OPEN ACCESS

Effects of Electrode Curvature in Li-Ion Cells

To cite this article: Robin Schäfer *et al* 2023 *J. Electrochem. Soc.* **170** 120519

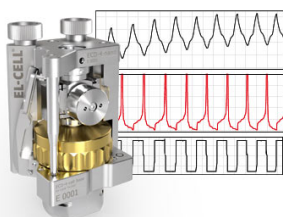
View the [article online](#) for updates and enhancements.

You may also like

- [State-of-Charge Dependence of Mechanical Response of Lithium-Ion Batteries: A Result of Internal Stress](#)
Wei Li, Yong Xia, Juner Zhu *et al.*
- [Energy Density of Cylindrical Li-Ion Cells: A Comparison of Commercial 18650 to the 21700 Cells](#)
Jason B. Quinn, Thomas Waldmann, Karsten Richter *et al.*
- [An Efficient Electrical Network Model for Computing Electrochemical State Distributions in a Spirally Wound Lithium-Ion Cell](#)
Jake Christensen, Somani Patnaik, David Cook *et al.*

Measure the Electrode Expansion in the Nanometer Range. Discover the new ECD-4-nano!


electrochemical test equipment



- Battery Test Cell for Dilatometric Analysis (Expansion of Electrodes)
- Capacitive Displacement Sensor (Range 250 μm , Resolution ≤ 5 nm)
- Detect Thickness Changes of the Individual Electrode or the Full Cell.

www.el-cell.com +49 40 79012-734 sales@el-cell.com





Effects of Electrode Curvature in Li-Ion Cells

Robin Schäfer,¹ Estefane Delz,² Michael Kasper,¹ Volker Knoblauch,² Margret Wohlfahrt-Mehrens,^{1,3} and Thomas Waldmann^{1,3,z}

¹ZSW—Zentrum für Sonnenenergie- und Wasserstoff-Forschung, Baden-Württemberg, D-89081 Ulm, Germany

²Hochschule Aalen—Technik und Wirtschaft, Institut für Materialforschung, D-73430 Aalen, Germany

³Helmholtz Institute Ulm for Electrochemical Energy Storage, 89081 Ulm, Germany

Bending of electrodes in certain cell designs (cylindrical cells or flat wound jellyrolls) leads to curved electrodes (curvature κ). For double side-coated electrodes, this curvature leads to convex and concave sides of the coating. In this work, we describe the effect of curved electrodes on the microstructure and aging. From a simple elastic model, we find that the porosities of the convex and concave sides of curved electrode coatings can deviate theoretically for first inner winding in a typical cylindrical cell in the order of $\pm 2\%$, respectively. The elastic model is compared with light microscopy images and Post-Mortem analysis revealing additional plastic deformation for small electrode bending radii. Electrode resistance measurements of the electrode coating as a function of winding radius is added to the overall context. The study concludes with an evaluation and discussion on typical bending radii of electrodes in different cell types (pouch, PHEV1, and 21700) and states (fresh, aged, and abused).

© 2023 The Author(s). Published on behalf of The Electrochemical Society by IOP Publishing Limited. This is an open access article distributed under the terms of the Creative Commons Attribution 4.0 License (CC BY, <http://creativecommons.org/licenses/by/4.0/>), which permits unrestricted reuse of the work in any medium, provided the original work is properly cited. [DOI: 10.1149/1945-7111/ad1304]



Manuscript submitted August 10, 2023; revised manuscript received October 26, 2023. Published December 18, 2023.

Cell design and electrode microstructure of Li-ion batteries are critical factors determining performance and aging behavior. Depending on their application, Li-ion cells are built in different formats.^{1,2}

While coin cells use flat electrodes with no curvature ($\kappa = 0 \text{ mm}^{-1}$), pouch and prismatic formats either utilize flat electrode stacks or flat-wound jellyrolls consisting of flat and curved parts.² In the simplest case of a flat electrode, e.g. in an electrode stack,³ the curvature is $\kappa = 0 \text{ mm}^{-1}$. However, if the electrodes are wound to jellyrolls, e.g. for prismatic or cylindrical cells, the curvature becomes $\kappa > 0 \text{ mm}^{-1}$.

We have recently developed a method to determine electrode curvatures from CT measurements.² In flat wound jellyrolls, the flat regions show in good approximation no curvature $\kappa = 0 \text{ mm}^{-1}$ while the curved regions are in the order of 0.16 mm^{-1} (outer part) to 7.1 mm^{-1} (inner part).²

Cylindrical cells use a rod-like mandrel to produce the jellyroll, resulting in an Archimedean spiral-like geometry.³⁻⁶ In some cases the mandrel remains in the jellyroll for mechanical stabilization.

The Archimedean spiral curve in polar coordinates is given by^{3,7,8}

$$r = a \cdot \theta \quad [1]$$

where the radius r defines the spiral line at a given polar angle $\theta > 0$. We note that the inner windings (e.g. in our scheme in Fig. 2a < 2100° , ~ 6 windings) are not existing due to center hole. The polar angle is multiplied by the factor a as follows^{3,8}

$$a = \frac{d_{\text{asc}}}{2\pi} \quad [2]$$

where d_{asc} is the sum of the thicknesses of one double side coated anode, two separators, and one double side coated cathode.^{2,3,9} This value was called “ d ” by Waldmann et al.⁹ in 2015 and later denoted d_{asc} ^{2,3} to determine the repetitive periodic distance within the jellyroll windings in a clearer way. For example, d_{asc} is known (among other factors) to have an influence on the heating behavior of 18650 cells.⁹

The curvature of windings of an electrode bent around a cylinder of radius r can be estimated by³

$$\kappa = \frac{1}{r} \quad [3]$$

consequently with the unit mm^{-1} .

For an Archimedean spiral, the electrode curvature can be described by^{3,8}

$$\kappa = \frac{\theta^2 + 2}{a(\theta^2 + 1)^{\frac{3}{2}}} \quad [4]$$

which approximates Eq. 3 for a given winding in the jellyroll. For example, when the inner windings in a jellyroll of a cylindrical cell are wound around a mandrel with a radius of 2 mm, the curvature becomes $\kappa = 0.5 \text{ mm}^{-1}$, as it can be seen by the dashed lines in Fig. 2a. In contrast, in the outermost windings of a cylindrical cell, type 21700, we observe $\kappa = 0.098 \text{ mm}^{-1}$.^{2,3}

While the performance and conductivity of a cell is determined by factors such as active material,¹⁰ electrode coating thickness,¹¹⁻¹³ porosity,¹¹⁻¹⁵ and tortuosity,^{12,16,17} it is also critical to understand the influence of these parameters on aging mechanisms.¹⁸⁻²³ Cell designs with a wound or flat-wound jellyroll can be produced at higher production speeds due to roll-to-roll processes compared to electrode stacking techniques.^{24,25} However, electrode bending has effects that are not well understood up to now. In a previous paper, we suggested that electrode curvature may lead to decompression and compression for the convex and concave sides of the electrode coating, respectively.³ However, materials typically show linear elastic behavior according to Hooke’s law for low strain values and non-linear inelastic deformation for higher strain values.²⁶ Initial observations by Mussa et al.²⁷ and from our group³ about different aging behavior of the convex and concave electrode coatings show the importance of this topic.

In this paper we investigate the effects of the electrode curvature on the microstructure and aging of Li-ion cells. We develop a straightforward theoretical elastic model, which is then compared with experimental data showing additional inelastic effects. The results are compared with resistivity measurements and Post-Mortem analysis of aged cells with curved electrodes. Finally, an overview of typical electrode curvatures evaluated from the literature is given.

Experimental

Theoretical porosity estimation of bent electrodes.—To calculate the theoretical porosity deviation that could occur within a jellyroll after the electrodes are wound, the inner (core facing) and

^zE-mail: thomas.waldmann@zsw-bw.de

outer (case facing) side coatings were compared. The inner side (concave) is compressed, while the outer side (convex) is stretched. The two sides form approximately concentric circles (cross-section of corresponding cylinder) with different radii (e.g., $r_{n,\text{an convex}}$ and $r_{n,\text{an concave}}$), and the base areas of the cylinder footprints can be calculated. Since the length of the electrodes is considered unchanged while bending, the areas can be used as approximation for the volumes. The percentage of deviation of both areas from the flat electrode is therefore a measure for the elastically created additional or decreased volume. Since the 3rd dimension can be considered constant, it cancels out in the ratio of both areas. This volume change is reflected in the porosity when the deformation is considered elastic.

Metallographic sample preparation.—For optical observation of microstructural changes due to compression and stretching of the electrode coatings, dry electrode samples (without electrolyte contact) were bent around rods of different radii, namely 10, 5, 2.5, and 1.25 mm (Fig. 1b). For even higher curvatures, electrodes were bent around plates (0.5 mm thick) with the following resulting radii: 1, 0.75, 0.5, and 0.25 mm (Fig. 1a). The curved specimens were initially cold-mounted with an epoxy resin from Struers (EpoFix), followed by a metallographic preparation. A flat and smooth surface, which is crucial to an accurate interpretation of the electrode microstructure, was achieved by grinding and polishing the specimens using a Struers Tegramin 30 automatic machine. A detailed description of the metallographic procedure has already been published previously.^{28,29}

Light microscopy.—A ZEISS Axio Imager Vario reflected-light microscope was used for all examinations. Images were acquired manually with an AxioCam HRc digital camera and processed using ZEN Core version 2.6 software. An overview of the individual specimens prepared is shown in Fig. 1.

Electrode composite volume resistivity measurements.—To approximate the curvature that occurs in the curved state inside a cell, the dry electrodes were moved back and forth over different mandrels to mimic their shape. This was done using the Elcometer 1500 instrument, which consists of cylindrical mandrels of different radii on a test stand. This procedure induces cracks and mechanical delamination to determine adhesion and elasticity/plasticity. The resistivity was then determined in the uncurved state ($\kappa = 0 \text{ mm}^{-1}$) using the HIOKI RM2610 Electrode Resistivity Measurement System. Nine measurements were taken at different positions of a 3×3 matrix to calculate the mean values and standard deviations of the electrode composite volume resistivity $\Delta\rho_{CV}$.

Electrochemical characterization and commercial cells.—Two different 21700 type cells were aged with BaSyTec systems. Cell A

is a commercial 21700 type cell with Ni-rich cathode with NMC + LiNiO₂ || graphite + ~1.8% Si chemistry aged for 300 C/2 cycles. The cathode coating thickness was ~80 μm on both sides of ~11 μm Al foil. The anode coating thickness was ~93 μm on both sides of ~11 μm Cu foil. The separator consists of ~12.6 μm Polyolefin (PE) with ~2.2 μm Al₂O₃ coating facing the cathode side. Cell B is of NMC622 || graphite chemistry produced at ZSW's pilot line and cycled for 3400 1 C cycles.

SEM measurements.—Cross-sections were prepared using a Hitachi IM4000Plus broad-beam argon ion milling system at 5 kV ion beam voltage. The aged electrodes were exposed to air during sample preparation. Scanning electron microscopy (SEM) measurements were performed with a Zeiss LEO 1530 VP equipped with a Gemini thermal field emission column. The secondary electron (SE) detector was operated at 5 kV.

CT measurements and curvature evaluation.—To evaluate the deformations that appear on curved electrodes, κ is obtained from X-ray computed tomography (CT) data from literature.^{2,30–41} Therefore, the respective regions of interest (high curvature) were evaluated by superposition of segmented lines in the ImageJ software. Using the scale from the CT data, the selected path was scaled and imported into Origin, where it was fitted with a polynomial. The minimum radius of curvature can be extracted by using Origin's curvature radius application, similar to Ref. 2.

Results and Discussion

Elastic model of curved electrodes.—Previous results suggest that electrode curvature could possibly lead to decompression and compression for the convex and concave coating sides, respectively.³ In a first approach, we develop a model of curved electrodes that does not consider irreversible plastic deformation.

In order to simplify the calculation, we take advantage of the fact that the curve shape and thus κ of a given electrode winding can be approximated by a circle (see Eqs. 3 and 4 and Fig. 2a). With the number of windings n , the thickness d_{asc} (see Eq. 2 and Fig. 2b),

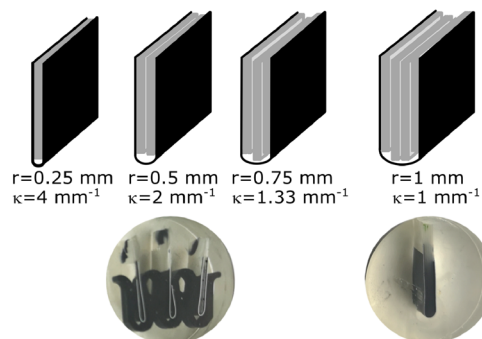
$$d_{\text{asc}} = d_{\text{an}} + 2d_{\text{sep}} + d_{\text{cat}} \quad [5]$$

and the radius (see Fig. 2c) of each circle is given by

$$r_n = r_{\text{core}} + n \cdot d_{\text{asc}} \quad [6]$$

where for $n = 0$, r_0 is equal to r_{core} , corresponding to the border between the electrode free center hole and the first winding of the electrode. More precisely, separating the inner electrode (here: anode) into inner and outer coating side, for $n \geq 1$ ($n \in \mathbb{N}$) the radius of the outer contour of the convex anode coating is determined by

a) bending around plates



b) bending around rods

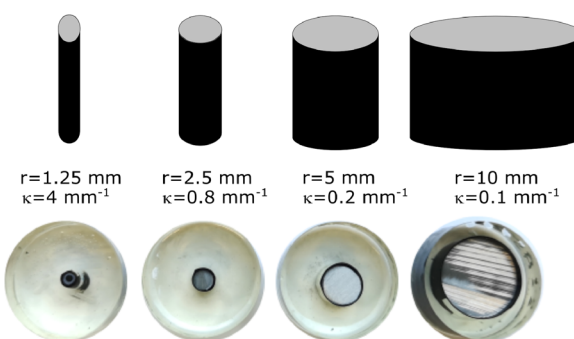


Figure 1. Scheme of the preparation of the curved electrodes for metallographic preparation and their cross-sections after the embedding process. The electrodes were bent around (a) different numbers of plates (0.25 mm thick) for radii between 0.25 and 1 mm and (b) rods of different radii between 1.25 and 10 mm.

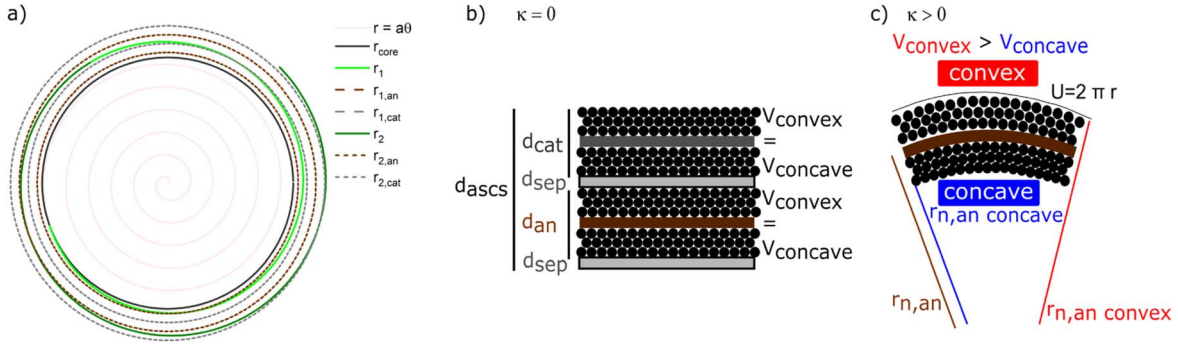


Figure 2. (a) The principle of approximating the Archimedean spiral by concentric circles, exemplary the superposition of the simplified first innermost anode and cathode of layer r_1 (brown and gray dashed lines) with $d_{asc} = 283 \mu\text{m}^6$ and the Archimedean spiral (bright and dark green lines). (b) Illustration of the repeating electrode layers without curvature and (c) curved anode with convex (red) and concave (blue) curved electrode surfaces with respective radii. Particle arrangement is schematically shown as periodic repetition.

$$r_{n,an\ convex} = r_{core} + n \cdot (d_{sep} + d_{an}) + (n - 1) \cdot (d_{sep} + d_{cat}) \quad [7]$$

with the thicknesses of anode d_{an} , cathode d_{cat} , and separator d_{sep} (see Fig. 2b). For the outer contour of the concave case, the anode thickness d_{an} needs to be subtracted, leading to

$$r_{n,an\ concave} = r_{core} + n \cdot d_{sep} + (n - 1) \cdot (d_{an} + 2d_{sep} + d_{cat}) \quad [8]$$

If one cathodic layer d_{cat} and one separator d_{sep} is added to Eq. 7, the radius of the outer electrode (here: cathode) is described by

$$r_{n,cat\ convex} = r_{core} + n \cdot (d_{an} + 2d_{sep} + d_{cat}) \quad [9]$$

for the outer convex cathode border. If one d_{cat} is subtracted from Eq. 9, it determines to

$$r_{n,cat\ concave} = r_{core} + n \cdot (d_{an} + 2d_{sep}) + (n - 1) \cdot d_{cat} \quad [10]$$

which describes the outer concave border of the cathode. The radius of the respective electrode middle (e.g. for the anode) is simply the mean value of $r_{n,convex}$ and $r_{n,concave}$

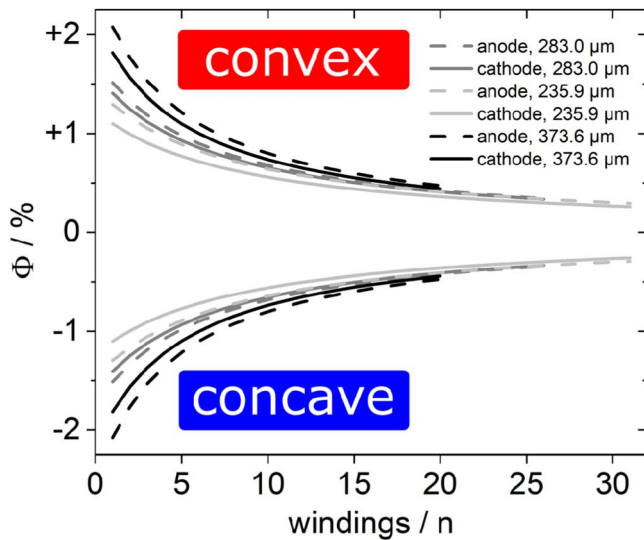


Figure 3. Calculated possible porosity deviation of curved anodes and cathodes in cylindrical cells for three different optimizations: high-power ($d_{asc} = 235.9 \mu\text{m}$), ($d_{asc} = 283 \mu\text{m}$)⁶, and high-energy ($d_{asc} = 373.6 \mu\text{m}$). The maximum winding number corresponds to the jellyroll of a 21700 type cylindrical cell. In this model, the coating thickness is assumed to stay constant while only the porosity changes.

$$r_n = \frac{r_{n,convex} + r_{n,concave}}{2} \quad [11]$$

We note that Eq. 11 corresponds to the middle of the current collecting foil, which thickness is neglected here. The area of interest (e.g. convex coating) is determined by the area difference of two consecutive circles

$$A_{n,convex} = \pi(r_{n,convex}^2 - r_n^2) \quad [12]$$

The uncompressed area of the flat unwound electrode is given by the circumference according to r_n and the half of the electrode thickness d

$$A_{n,flat} = 2\pi \cdot r_n \cdot \frac{d}{2} = \pi \cdot r_n \cdot d \quad [13]$$

If the convex area $A_{n,convex}$ is divided by the flat area $A_{n,flat}$, the porosity deviation (convex to flat) within one electrode is calculated by

$$\frac{A_{n,convex}}{A_{n,flat}} = \frac{\pi(r_{n,convex}^2 - r_n^2)}{\pi \cdot r_n \cdot d} = \frac{r_{n,convex}^2 - r_n^2}{r_n \cdot d} \quad [14]$$

leading to the porosity change within one electrode coating, compared to the flat electrode (Φ_{flat}), since an increasing area is accompanied by an increased porosity.

If the convex area $A_{n,convex}$ is divided by the concave area $A_{n,concave}$, the porosity deviation (convex to concave) within one electrode is calculated by

$$\Delta\Phi_{\pm} = \frac{A_{n,convex}}{A_{n,concave}} = \frac{\pi(r_{n,convex}^2 - r_n^2)}{\pi(r_n^2 - r_{n,concave}^2)} = \frac{r_{n,convex}^2 - r_n^2}{r_n^2 - r_{n,concave}^2} \quad [15]$$

The possible porosity deviation for convex and concave to the flat state is given by

$$\Phi(r_n) = \begin{cases} \Phi_{flat} + \frac{\Delta\Phi_{\pm}}{2}, & n \geq 1, n \in N, \text{convex} \\ \Phi_{flat} - \frac{\Delta\Phi_{\pm}}{2}, & n \geq 1, n \in N, \text{concave} \end{cases} \quad [16]$$

The calculated results using Eq. 16 are shown in Fig. 3 for three exemplary layer thicknesses d_{asc} from the literature: $235.9 \mu\text{m}$ (high-power cell), $283 \mu\text{m}$, and $373.6 \mu\text{m}$ (high-energy cell). As the innermost layer (r_1) has the highest curvature, the highest possible porosity deviation $\Delta\Phi$ is observed. As the number of electrode windings increases, $\Delta\Phi$ approaches 0, which is depicted in Fig. 3. The plotted lines in Fig. 3 show $\Delta\Phi$ within the considered electrode pairs of different layer thicknesses d_{asc} , compared to the

uncompressed layer. For example, for the first layer (r_1) with thickness $d_{\text{asc}s} = 283 \mu\text{m}$ the porosity deviation between the convex and the concave coating side of the inner electrode (here: anode) of first layer ($n = 1$) is 3.03%. Through the slightly higher radius of the outer electrode (here: cathode), the deviation is slightly smaller (2.81%). Expressed by Eq. 16, this corresponds to $\Phi_{\pm, \text{an}} = \pm 1.5\%$ for anode and $\Phi_{\pm, \text{cat}} = \pm 1.4\%$ for cathode.

Remarkably, the thickness $d_{\text{asc}s}$ of the electrode affects the (de-)compression per layer. For instance, in Fig. 3 we find $\Phi_{\pm, \text{an}} = \pm 1.3\%$ and $\Phi_{\pm, \text{cat}} = \pm 1.1\%$ for $d_{\text{asc}s} = 235.9 \mu\text{m}$, $\Phi_{\pm, \text{an}} = \pm 2.1\%$ and $\Phi_{\pm, \text{cat}} = \pm 1.8\%$ for $d_{\text{asc}s} = 373.6 \mu\text{m}$, respectively. This indicates the trend that thicker electrodes are affected more strongly compared to thinner electrodes.

While Fig. 3 shows the elastic change of porosity under the assumption of no thickness change of the electrode coating, the solid lines in Fig. 4a show the elastic thickness change of the coating without porosity change. The calculation is based on Eq. 15.

$$\Delta d_{\pm} = \frac{A_{n, \text{convex}}}{A_{n, \text{concave}}} = \frac{\pi (r_{n, \text{convex}}^2 - r_n^2)}{\pi (r_n^2 - r_{n, \text{concave}}^2)} = \frac{r_{n, \text{convex}}^2 - r_n^2}{r_n^2 - r_{n, \text{concave}}^2} \quad [17]$$

with r_n as given in Eqs. 7–10. It is noted that the y -axis (change of coating thickness) is mirrored compared with Fig. 3 (porosity) regarding the convex and concave curves. Thus, the increase in area of the stretched convex coating is accompanied by a thickness decrease at constant porosity. On the other hand, the compressed concave coating needs to increase thickness in order to maintain the porosity. By this, the results are determined by Eq. 18

$$d(r_n)_{\pm} = \begin{cases} d_{\text{flat}} - \frac{\Delta d_{\pm}}{2}, & n \geq 1 \ n \in N, \text{ convex} \\ d_{\text{flat}} + \frac{\Delta d_{\pm}}{2}, & n \geq 1 \ n \in N, \text{ concave} \end{cases} \quad [18]$$

We note that these changes in the electrode microstructure are theoretical values and are difficult to measure, especially for the porosity. For example, in Hg porosimetry measurements with single side coated curved electrodes, no differences were measurable within the error range. However, this calculation indicates that there are likely differences in a region of κ where the electrodes behave elastically.

Inelastic deformations of curved electrodes.—In the theoretical model above, the electrode coating is expected to behave elastically. I.e. with pure elastic behavior, the electrode porosity and/or the

thickness will consequently change with compression without plastic deformation. In the case of inelastic behavior, the porosity, thickness, and integrity of the electrode coating may change irreversibly. This is observed below, using metallographic cross-sections of curved electrodes. In this way, the experimental results can be compared with the elastic model described in the previous section. Figure 4b shows the metallographic preparation of a curved cathode for the example of $\kappa = 4 \text{ mm}^{-1}$. From such measurements, the coating thickness can be measured directly. Figure 4a shows the thickness variation for the convex and concave side of the coating as a function of the bending radius r . We find a reasonable agreement between the elastic model with thickness variation (blue line in Fig. 4a) and the experiments (blue circles in Fig. 4a) for the concave side of the coating. Figure 4b reveals that the thickness change of the concave side of the coating is caused by cathode particles being pushed out of the coating due to compression.

For the convex side of the cathode coating, the experimental data (red squares) show a reasonable agreement with the model (red line) for $\kappa \leq 2 \text{ mm}^{-1}$. However, for larger curvatures, the experimental data clearly deviate from the model, as the thickness of the convex side does mostly not change with κ in most cases. As shown in Fig. 4b, the convex side appears to be relieved of bending stress by various effects, such as porosity change as described in the elastic model with porosity change at constant thickness (Fig. 3).

The anode in Fig. 5 shows similar trends as already observed for the cathode (Fig. 4). The concave coating shows an almost homogeneous thickness increase with κ , similar to the expectation based on the theoretical elastic model with constant porosity and varying thickness (Fig. 5a). For the cathode, this thickness increase is mainly due to active material particles being pushed out of the coating by the compression caused by the electrode bending.

For the convex side of the anode coating, the thickness remains approximately constant (Fig. 5a). This is similar to the cathode (Fig. 4). There is reasonable agreement between the experimental data (red squares in Fig. 5a) and the elastic model, given for $\kappa \leq 0.8 \text{ mm}^{-1}$ in the case of the anode. For larger curvatures, the data show a clear deviation from the elastic model at constant porosity and varying coating thickness. This finding is also in agreement with the observations on the cathode. In contrast, the anode (Fig. 5) appears to relieve the bending stress locally through perpendicular cracks in the convex coating. As it can be seen in Fig. 5b, the convex anode coating fractures into brittle segments while maintaining flat parts of the surface. This results in large cracks and visible island formation, different from the behavior of the cathode.

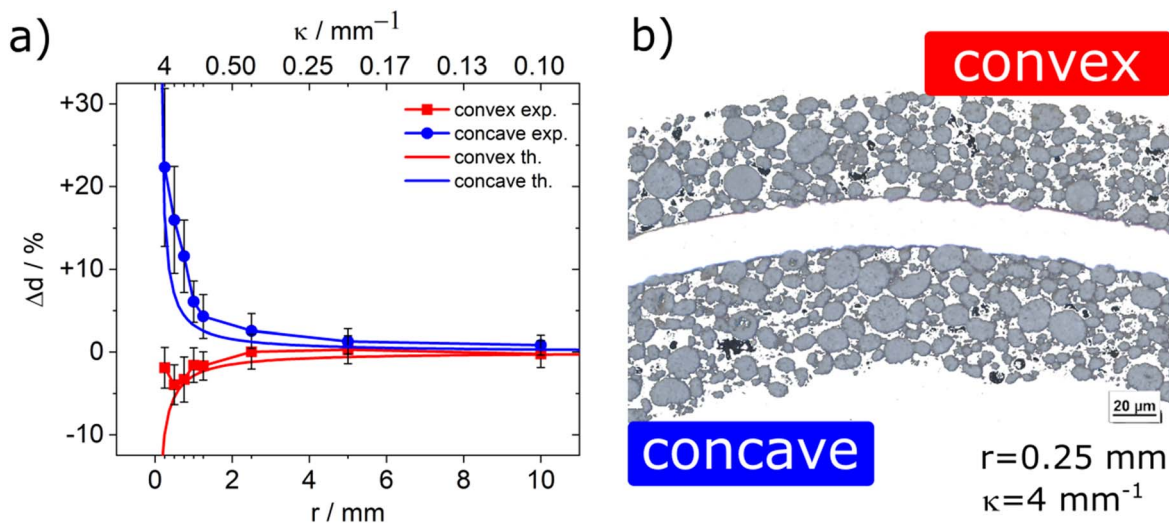


Figure 4. (a) Combination of the theoretical elastic model for thickness change of the cathode without porosity change (solid lines) with experimental data of the cathode (data points). (b) Exemplary light microscopy recording of a metallographic preparation of the highest tested curvature value $\kappa = 4 \text{ mm}^{-1}$ for winding around $r = 0.25 \text{ mm}$. The electrode was isolated from the background by color identification.

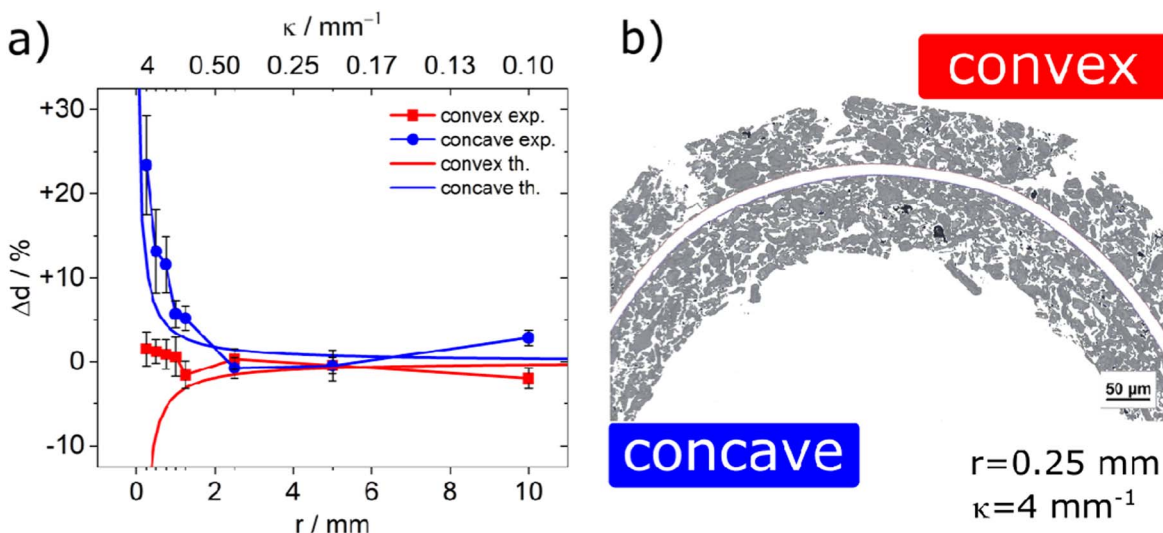


Figure 5. (a) Experimental thickness variation (data points) of the anode in combination with the theoretical elastic model for thickness change (solid line) without porosity change. (b) Light microscopy image of the highest curvature at the smallest radius of 0.25 mm. The electrode was isolated from the background by color identification.

As shown by Üçel et al.⁴² the mechanical behavior of the graphite anode is mainly governed by the porosity and the binder due to the low values of Young's modulus compared to the particle stiffness.⁴² This behavior is also assumed for the cathode, since the particle stiffness is even higher and no intraparticle cracking was observed in our work. Further, the cohesion of the cathode's particle binder network is obviously higher, since no interparticle cracks are observed as for the convex anode coating (compare Figs. 4b and 5b). The resistance against compressive stress (concave coatings) is given by the strength of the particles, rather than the binder particle cohesion. In addition, the Young's modulus in compression is larger than that in tension, highlighting the more severe damage to the concave sides of the coating.^{42,43} Their method also captured the hysteresis effect in tension and compression, due to the polymeric binder and the formation of new microstructural contacts.⁴²

The NMC cathode material particles of Gupta et al.⁴³ exhibit much greater particle stiffness, while the anode coating is stiffer in compression compared to the cathode coating. This agrees with our findings, particularly with our electrode formulation, that the anode is unable to follow the shape while bending in the same way as the cathode and exhibits pronounced cracking.⁴² Therefore, the anode experiences more targeted stress relief (island formation), while the coating thickness remains relatively constant. The reality is most likely a superposition of the described changes in porosity, coating, thickness, and deformations.

Figure 6 shows the behavior of anodes and cathodes for different curvatures in the range of 4 mm^{-1} to 0.1 mm^{-1} . For $\kappa = 4 \text{ mm}^{-1}$, the convex side of the anode (Fig. 6a) again clearly shows crack formation (Fig. 6a), while no cracks are observed for the convex side of the cathode (Fig. 6d). For $\kappa = 4 \text{ mm}^{-1}$, particles are again pushed out of the coating of the anode (Fig. 6a) and cathode (Fig. 6d) for the concave side. In contrast, for $\kappa = 0.8 \text{ mm}^{-1}$ (Figs. 6b, 6e) and $\kappa = 0.1 \text{ mm}^{-1}$ (Figs. 6c, 6f), neither the anode nor the cathode shows any cracks or pushed out particles. This is expected since the stress is very low. The small effect of the electrode bending for $\kappa \leq 0.8 \text{ mm}^{-1}$ is also evident from Figs. 6b–6c, 6e–6f, where the electrodes do not look curved on the small observed length scale of $\sim 250 \mu\text{m}$. Schilling et al.⁴⁴ found the threshold curvature for the onset of deformation to be $\kappa > 3 \text{ mm}^{-1}$. At $\kappa = 6.7 \text{ mm}^{-1}$ an increase in surface roughness and even delamination was observed.⁴⁴ These values are in a similar range as in Fig. 6, however, it has to be kept in mind that the electrodes are different in our study and in Schilling et al.

These observations have implications for the inner and outer windings of cylindrical cells. The outer windings of cylindrical (18650, 21700, and 48600) or prismatic (PHEV1 and PHEV2) cells, or for even larger formats, usually do not suffer from inelastic deformations of the electrode coatings. This is similar for electrode coils (with even lower κ values) after electrode production or for stacked electrodes ($\kappa = 0 \text{ mm}^{-1}$). However, inelastic deformations may come into play for the inner windings of jellyrolls in cylindrical cells or cells with flat-wound jellyrolls. Finally, kinked electrodes (very high κ values) suffer mostly from inelastic deformations.

We have recently shown that the addition of inner windings (with high κ values) to cylindrical cells does not lead to a significant increase in the capacity.³ For example, in a high-energy 18650 cell with 3.99 Ah, filling the inner cylinder with additional electrodes would add only 0.18 Ah of capacity.³ This is equivalent to a 4.3% increase in capacity and includes κ values of up to 2.5 mm^{-1} for high-energy cells ($d_{\text{asc}} = 391.6 \mu\text{m}$).³ For high-power cells ($d_{\text{asc}} = 253.9 \mu\text{m}$), κ in the core region (which is typically left empty) can be as high as 5 mm^{-1} .³ As shown in Fig. 6, this can already be in the region of inelastic electrode deformation.

In contrast, adding about half of an outer winding results in +0.164 Ah in case of a high-energy cell.³ This corresponds to an increase of 3.9% in capacity, which is in a similar range as adding inner windings. However, the outer windings are mostly without risk of inelastic deformation due to low electrode curvature (Fig. 6). It should be noted that additional outer windings in cylindrical cells necessitate an increase in cell dimensions, which is often observed in commercial high-energy cylindrical cells (for the given example an increase of $\sim 400 \mu\text{m}$ in cell diameter).

Composite volume resistivity.—Electrode composite volume resistivity ρ_{CV} measurements after bending of the electrodes are evaluated in this section. Since ρ_{CV} is measured in a flat state, only irreversible plastic deformation can be measured in our setup. Consequently, the electrodes were bent to values of κ and then bent back to $\kappa = 0 \text{ mm}^{-1}$ where the $\Delta\rho_{\text{CV}}$ (difference of ρ_{CV} before and after bending) measurements were conducted. Figure 7 shows $\Delta\rho_{\text{CV}}$ as a function of previous κ values.

The convex cathode coating (gray circles in Fig. 7, right-hand side) shows an increase in $\Delta\rho_{\text{CV}}$ of up to +30% at $\kappa = 4 \text{ mm}^{-1}$. In contrast, the concave cathode coating (gray circles in Fig. 7, left-hand side) shows the largest increase of $\Delta\rho_{\text{CV}}$ (up to 140% increase). The rearrangement of the particles due to compressive

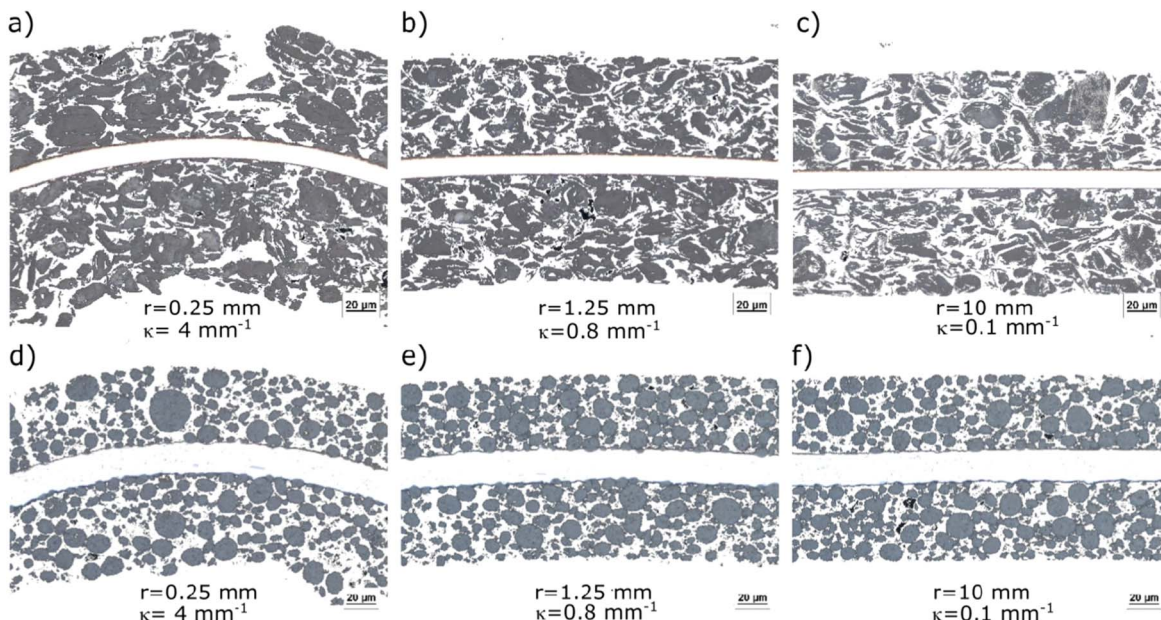


Figure 6. Light microscopy images of curved anodes (a)–(c) and cathodes (d)–(e) at different curvatures. The electrode was isolated from the background by color identification.

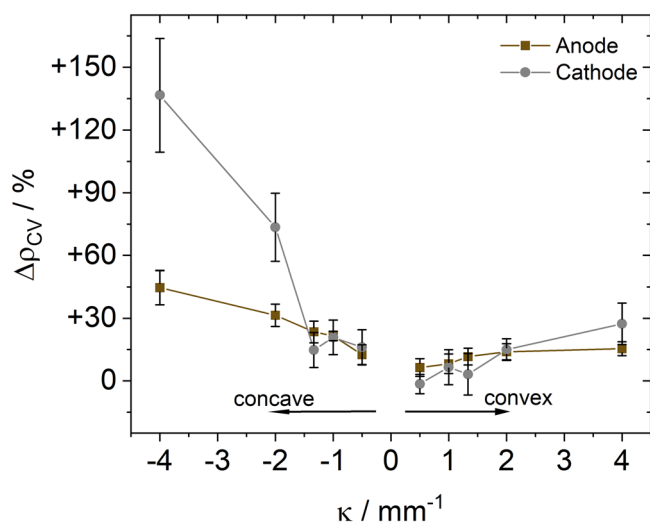


Figure 7. Relative increase of electrode composite volume resistivity $\Delta\rho_{CV}$ as a function of applied curvature.

stress and the resulting increase in thickness cannot be buffered by the cathode coating as well as by the anode coating (see Fig. 7).

The convex anode coating (brown squares in Fig. 7, right-hand side) is less affected by the curvature of up to $\kappa = 4 \text{ mm}^{-1}$, indicated by an increase of $\Delta\rho_{CV}$ by only +15%. Remarkably, the cracks through the entire convex anode coating (brown squares in Fig. 7, left hand side) do not affect $\Delta\rho_{CV}$ as much as much as might be expected from Fig. 5b. The data suggest that the electrical contact of the surfaces of the cracks is increased when they are compressed by bringing the electrode back to the flat state.

Although the concave anode coating (brown squares in Fig. 7, left-hand side) shows a +45% increase in $\Delta\rho_{CV}$, it is much less than the concave cathode ($\Delta\rho_{CV} = +140\%$, gray circles in Fig. 7, left-hand side). However, both directions of curvature affect the particle contact within the network, increasing the electronic resistivity after bending.

Post-Mortem analysis.—Figures 8a, 8b show SEM measurements of cross-sections of unwound aged electrodes (cell A) from the core-near regions after 300 cycles, corresponding to $\sim 93\%$ SOH. The microstructure of the cathode in Fig. 8a is decompressed on the concave side. The scale in the graph shows a thickness increase of up to $\sim 44\%$ of the thickest position on concave side, compared to the thinnest position of the convex side (see Fig. 8a). We note that the observed thickness increase and the cracks in the electrode coating might have been reinforced by the cell opening stress.

Figures 8a, 8b indicate a different aging behavior on the concave side, as the convex side resisted the stress of cell opening. In contrast, the concave side was inelastically deformed in the form of electrode cracks. The observed difference could also be explained by only different swelling, based on effects of (de-)compression. On the other hand, due to unrolling the cracks on convex coatings could be closed (referred to low electronic resistivity increase on convex anode although strong cracks, see Figs. 5b, 6a, 7), while on the concave coatings the cracks appear only when unwinding.

Also for the anode in Fig. 8b, the concave side shows more aging, but in the form of cracks. The increase in thickness is up to $\sim 17\%$ (see Fig. 8b, if the thickest position on concave side is compared to the thinnest position of the convex side). Appearing rather due to delamination by cracking than to decompression. We would like to mention that it is unclear whether the cracks appear after unwinding the electrodes, due to the mechanical stress, or whether they are already present in the closed cell. The cracks may already be present in the closed cell, e.g. due to volume changes during charging and discharging.⁴⁵ As shown by Figs. 8c–8f, no structural changes are visible on macroscopic level, neither on concave (Figs. 8c, 8e) nor on convex coatings (Figs. 8d, 8f). Figure 7 suggests that if these electrode cracks are already present in the closed cell, however, they do not necessarily lead to a drastic increase in cell resistance, since the crack surfaces are pressed together in the cell. This assumption can be drawn from the fact, that the size of the testing probe of the HIOKI measurement system is roughly 1 mm^2 , covering the μm -sized cracks by at least one order of magnitude. However, when the cells are opened and the jellyrolls are unrolled, the cracks are likely to develop to the stage observed in Fig. 8. Compared to the average thickness of the fresh electrodes, the convex cathode side decreases by $\sim 4\%$, while the concave side increases by $\sim 32\%$. The convex

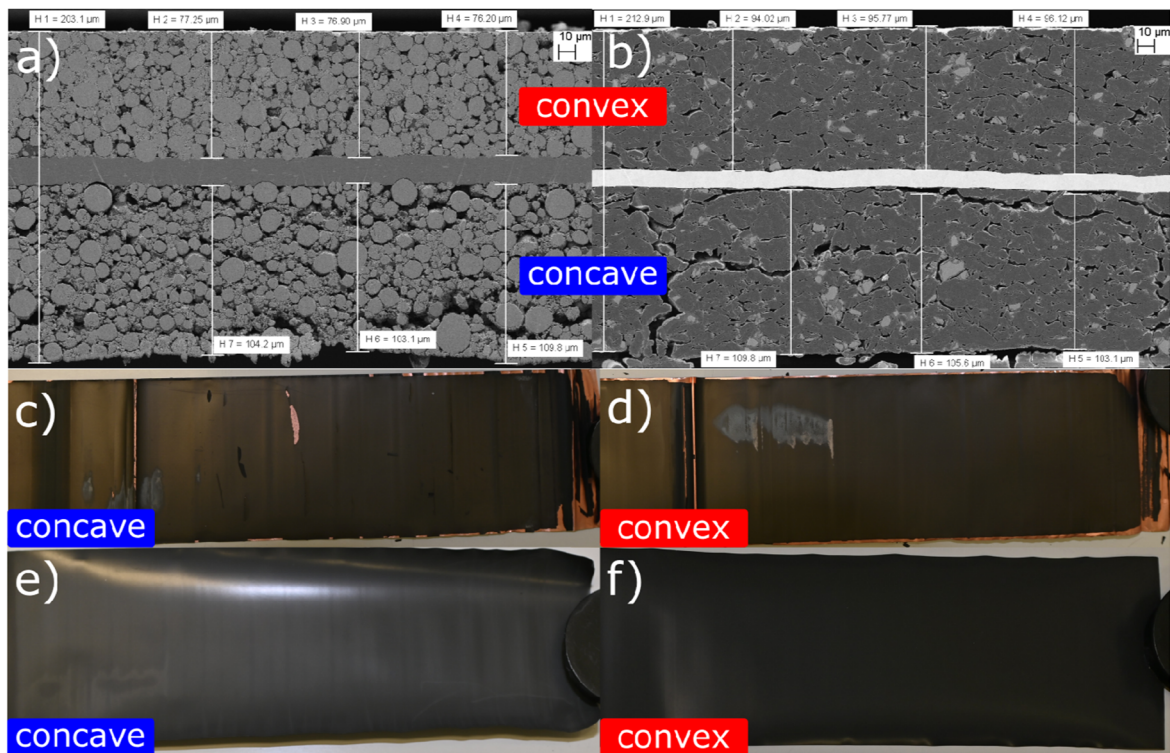


Figure 8. SEM of a cross-section of (a) cathode and (b) anode from cell A after 300 cycles. Photographs of (c) concave anode, (d) convex anode, (e) concave cathode, and (f) convex cathode. All images are from core-near regions.

anode coating increases on average by $\sim 3\%$ and the concave one by $\sim 14\%$. These thickness rises are consistent with the trends for convex and concave coatings observed in Figs. 4 and 5, where concave thickness increases and convex coatings remains rather unchanged. Nevertheless, the decompressed concave coatings are in contrast to the scheme in Fig. 2c (theoretical model of elastic porosity change), where the concave sides are predicted to be compressed by losing porosity.

Possible consequences could be an increase in tortuosity, which is a critical parameter for the aging behavior. In addition, mechanical changes could reduce the capacity and performance of the electrode through delamination (see Figs. 10c, 10d), Lithium consumption by SEI formation, and loss of mechanical integrity within the particle network of the electrodes.^{1,19,33,46} This is supported by Fig. 9, where the voltage profile of the 1st (black curve) and the 300th cycle (red curve) is compared. The overpotential is increased with cycles and the capacity is reduced, which is in accordance by the aging mechanisms discussed above. However, the aging mechanism cannot be determined from the voltage profiles only. This shows the importance of understanding the influence of the microstructure on aging and the changes of microstructure during aging.

Figure 10 shows the separator of cell B and which electrode side it is facing to in each case, allowing the coating detachment and adhesion to the separator to be traced. It is noteworthy that this strong delamination occurred after 3400 cycles. Obviously, the electrode delamination and adhesion to the separator appears to be higher on the concave side (Figs. 10b, 10d) than on the convex side (Figs. 10a, 10c), indicating higher mechanical stress due to aging on the concave coating side. In addition, the porosity reduction measured by Hg intrusion porosimetry in the anode is higher in the innermost regions near the core ($\approx 8\%$) than in the outermost windings near the cell housing ($\approx 3\%$), coinciding with the theoretical elastic model of porosity change (see Fig. 3), its combination with real data (Figs. 4a and 5a), and the literature.⁴⁷

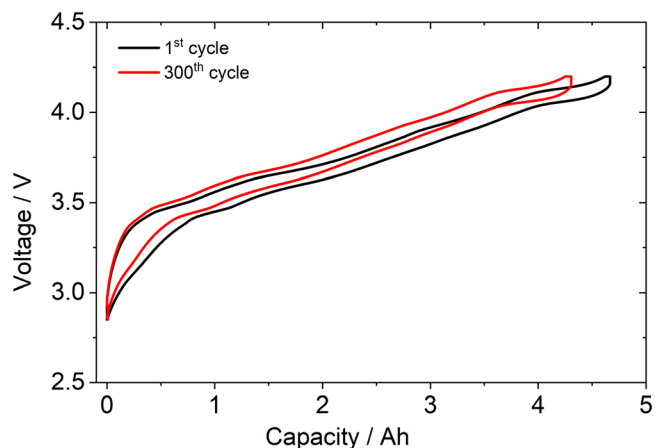


Figure 9. Voltage profile of 1st and 300th cycle of cell A.

Typical electrode curvatures in Li-ion cells.—The previous section emphasizes the importance of understanding the mutual influence of aging on the microstructure and the influence of microstructure on aging. In this section, typical curvatures reported in the literature are evaluated.

Figure 11 shows examples from curved electrodes in Li-ion cells from literature.^{2,35} Our evaluation is based on CT measurements and metallographic cross-sections.^{2,30–41} The data were evaluated by determining the maximum curvatures occurring in the electrodes (circles in Fig. 11, as they are expected to be the weakest points for further aging). The overview in Fig. 12 shows additional values which we evaluated from literature data.^{2,30–41} For clarity, the state of the cells (e.g. aged, subjected to different types of abuse methods) are categorized and color coded in Figs. 11 and 12.

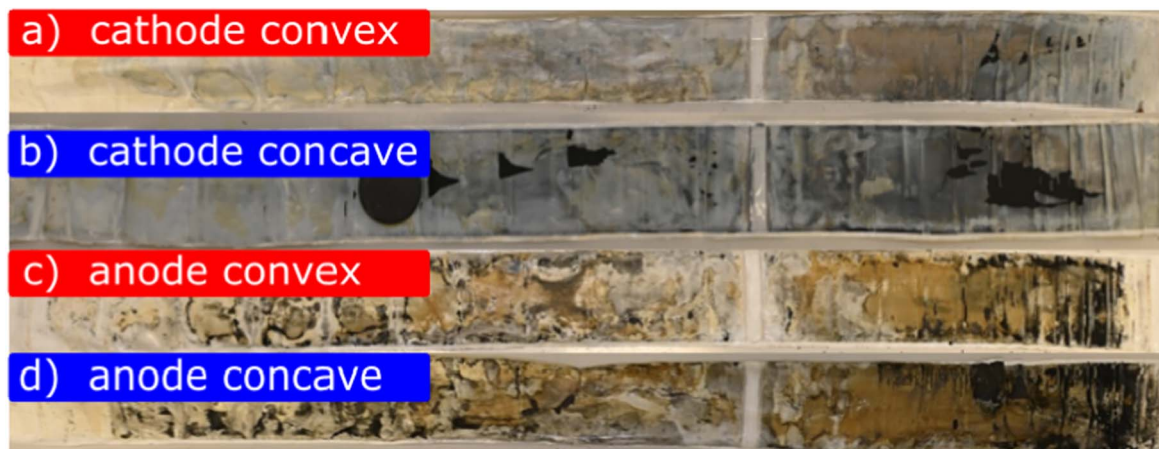


Figure 10. The separator of cell B after 3400 cycles facing different sides of the electrode coating. Delaminated material from (a) convex and (b) concave cathode side, (c) convex and (d) concave anode coating side. The innermost, core near regions are on the right hand side.

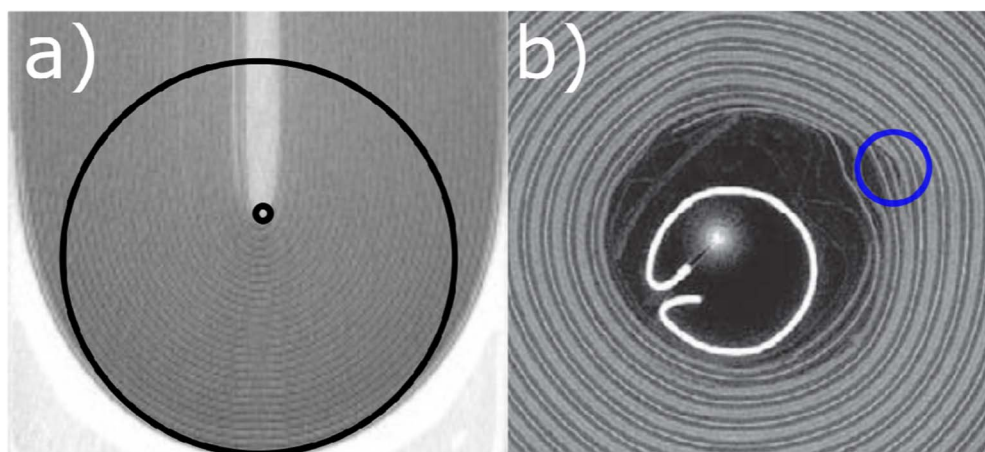


Figure 11. Exemplary evaluation of curvatures. Circles (color coded as in figure 12) represent the radii for determination of curvatures at the respective positions of evaluation. (a) Pristine PHEV cell.² (b) Thermally abused cylindrical cell of 18650 type.³⁵ Reprinted with permission.

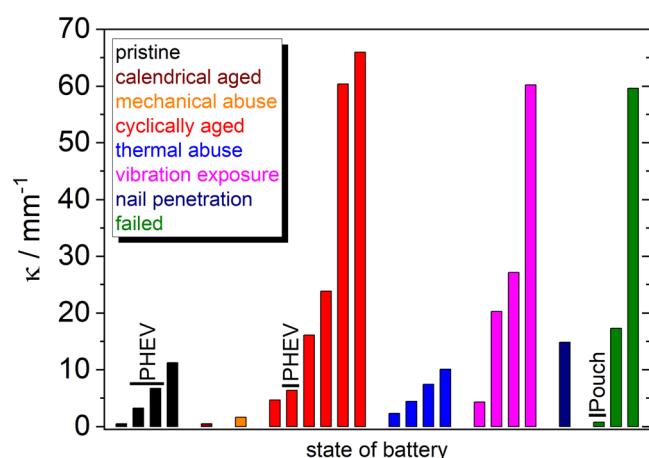


Figure 12. Overview of electrode curvatures of different battery states (color coded as in figure 11) found in the literature.^{2,30-41} Cylindrical cells unless otherwise noted.

As expected, pristine cells (black) show that lowest κ -values (0–11.24 mm⁻¹). The highest value in this evaluation for pristine cells of $\kappa = 11.24$ mm⁻¹ originates from deformations in a commercial cylindrical cell,³⁰ which clearly shows possible

deviations in real cells from the theoretical mathematically perfect value of $\kappa = 0.5$ mm⁻¹.²

Cycling aging (red) shows the widest range of curvatures (4.61–65.94 mm⁻¹),^{32,36-38,41} which is due to deformations of the jellyroll formed during aging. Such deformations of the jellyroll can lead to an increase of electrode curvature by about two orders of magnitude, compared to pristine cells. This is an important finding since these values are one order of magnitude higher than that, determined as persistent mechanical damage of $\kappa \approx 1$ mm⁻¹, identified by light microscope images in Fig. 6 and $\Delta\rho_{CV}$ measurements in Fig. 7. In contrast, three types of calendar aged cells (brown in Fig. 12) did not show such deformations of the jellyroll in a previous study of our group, most likely due to the absence dilation of the electrodes.⁹

Thermal abuse (blue) values of cylindrical cells are far below this range (2.35–10.08 mm⁻¹),³⁵ probably due to the possibility of venting in cylindrical cells. Nail penetrated (14.87 mm⁻¹),³³ mechanically abused (1.67 mm⁻¹),³⁴ and vibrationally tested (4.27–60.21 mm⁻¹)⁴⁰ cells are in the range already covered by cycling aged cells. Cells failed due to unknown history showed curvatures in the range of 0.75–59.63 mm⁻¹.^{31,39} We would like to mention that the lowest value for the failed cells corresponds to a ballooned pouch cell due to gas evolution.³¹ Our evaluation shows that in failed or abused cells, electrode material ablation can occur depending on the type of safety trigger, which likely has consequences on the ejected material in thermal runaway.

Conclusions

Winding of electrodes in cylindrical and flat-wound jellyrolls leads to curved electrodes (curvature κ). For double side-coated electrodes, this curvature leads to convex and concave sides of the coating. The effects of curved electrodes on microstructure and aging were investigated in this paper.

A theoretical consideration (elastic model) of curved electrodes led to the possibility of $\pm 2\%$ porosity or thickness changes on both coating sides of one electrode, respectively. Experiments with anodes and cathodes wound around rods with defined radii in combination with metallographic preparations confirmed the elastic model partially (thickness change at constant porosity) for the concave sides of the electrode coatings. In contrast to the theoretical elastic model, particles are pushed out of the concave coating side and additional cracks were observed on the convex coating sides of the anodes in case of high curvatures in the experiments.

The results are supported by electrode composite volume resistivity ρ_{CV} measurements in which the electrodes are bent to a certain curvature κ and then measured bent back to the flat state ($\kappa = 0 \text{ mm}^{-1}$). We found the tendency of $\Delta\rho_{CV}$ increasing with κ . The strongest increase in $\Delta\rho_{CV}$ was observed for a concave cathode for $\kappa \geq 1.3 \text{ mm}^{-1}$. In contrast, $\Delta\rho_{CV}$ was minor for convex anodes and cathodes up to $\kappa = 4 \text{ mm}^{-1}$. This can be explained by the fact that the cracked surfaces are pressed together for $\kappa = 0 \text{ mm}^{-1}$ where the ρ_{CV} was measured. This is most likely similar in a cell before disassembly.

In case of Post-Mortem analysis it has to be taken into account that the cell opening stress might change the microstructure and increase cracks in the electrodes. Post-Mortem analysis of cyclically aged commercial cylindrical cells and cells from our pilot-line confirmed different adhesion behavior and crack formation for anodes and cathodes on the convex and concave side of the electrode coatings.

Finally, our extended evaluation of CT measurements and metallographic cross-sections from literature show the range of occurrence and relevance of curved electrodes.

In reality there is most likely a mixture of the two extreme cases of the elastic model, thickness or porosity change, and inelastic deformations depending on the electrode composition. The effects of low curvatures are negligible, e.g. for outer windings of cylindrical cells (18650, 21700, 46800, and larger formats) or in roll-to-roll processes where large coils are used. Critical are high curvatures, e.g. if kinks occur in flat-wound jellyrolls or in deformed jellyrolls in cylindrical cells after cycling aging or in damaged cells. We note that the observed trends are most likely general, however, the exact κ -values depend on the electrodes, their recipe, and production process. The found trends are likely to be applicable to battery chemistries beyond Li-ion batteries, e.g. Na-ion batteries.

Our observations give valuable insights into mechanical changes which have effects on aging, e.g. by electrically disconnected particles in strongly curved parts of electrodes. This work emphasizes the importance of understanding the influence of these effects on the interplay of cell design, performance, aging, and safety. Further work in this direction is ongoing in our labs.

Acknowledgements

ZSW acknowledges funding of the projects MiCha (03XP0317C) in the Aqua-Cluster and RollBatt (03XP0245A) in the ProZell-Cluster by the German Federal Ministry of Education and Research (BMBF). Hochschule Aalen acknowledges funding of the project MiCha (03XP0317A). Project management by Forschungszentrum Jülich (PtJ) is gratefully acknowledged. The authors thank the ZSW members M. Feinauer for helpful discussions, C. Pfeifer for cross-section preparation and SEM measurements, K. Fischinger for Hg intrusion porosimetry measurements, as well as A.A. Regalado for helpful discussions.

ORCID

Robin Schäfer  <https://orcid.org/0000-0002-5204-5388>

Thomas Waldmann  <https://orcid.org/0000-0003-3761-1668>

References

- G. Bridgewater, M. J. Capener, J. Brandon, M. J. Lain, M. Copley, and E. Kendrick, *Batteries*, **7**, 38 (2021).
- T. Waldmann, S. Rössler, M. Blessing, R. Schäfer, R.-G. Scurtu, W. Braunwarth, and M. Wohlfahrt-Mehrens, *J. Electrochem. Soc.*, **168**, 90519 (2021).
- T. Waldmann, R.-G. Scurtu, K. Richter, and M. Wohlfahrt-Mehrens, *J. Power Sources*, **472**, 228614 (2020).
- Y. Xie, J. Kim, W. Na, Z. Feng, and S.-B. Son, *Meet. Abstr.*, **MA2022-01**, 445 (2022).
- J. B. Quinn, T. Waldmann, K. Richter, M. Kasper, and M. Wohlfahrt-Mehrens, *J. Electrochem. Soc.*, **165**, A3284 (2018).
- M. Guo and R. E. White, *J. Power Sources*, **250**, 220 (2014).
- D. A. McCleary, J. P. Meyers, and B. Kim, *J. Electrochem. Soc.*, **160**, A1931 (2013).
- From MathWorld—A Wolfram Web resource, Archimedes' spiral (10/2023), <https://wolframalpha.com/input?i=Archimedes%27+spiral>.
- T. Waldmann, G. Bisle, B.-I. Hogg, S. Stumpp, M. A. Danzer, M. Kasper, P. Axmann, and M. Wohlfahrt-Mehrens, *J. Electrochem. Soc.*, **162**, A921 (2015).
- C. P. Aiken, E. R. Logan, A. Eldesoky, H. Hebecker, J. M. Oxner, J. E. Harlow, M. Metzger, and J. R. Dahn, *J. Electrochem. Soc.*, **169**, 50512 (2022).
- C. Heubner, A. Nickol, J. Seeba, S. Reuber, N. Junker, M. Schneider, and A. Michaelis, *J. Power Sources*, **419**, 119 (2019).
- A. Adam, K. Huber, E. Knobbe, D. Griebel, J. Wandt, and A. Kwade, *J. Power Sources*, **512**, 230469 (2021).
- Z. A. Khan, M. Agnaou, M. A. Sadeghi, A. Elkamel, and J. T. Gostick, *J. Electrochem. Soc.*, **168**, 70534 (2021).
- J. Song, J. Kim, T. Kang, and D. Kim, *Sci. Rep.*, **7**, 42521 (2017).
- H. Xie, Y. Kang, H. Song, and Q. Zhang, *J. Power Sources*, **424**, 100 (2019).
- J. Landesfeind, J. Hattendorff, A. Ehrl, W. A. Wall, and H. A. Gasteiger, *J. Electrochem. Soc.*, **163**, A1373 (2016).
- K. S. Mayilvahanan et al., *J. Electrochem. Soc.*, **168**, 70537 (2021).
- A. Barré, B. Deguilhem, S. Grolleau, M. Gérard, F. Suard, and D. Riu, *J. Power Sources*, **241**, 680 (2013).
- J. Holloway, F. Maddar, M. Lain, M. Loveridge, M. Copley, E. Kendrick, and D. Greenwood, *Batteries*, **6**, 57 (2020).
- M. Wohlfahrt-Mehrens, C. Vogler, and J. Garche, *J. Power Sources*, **127**, 58 (2004).
- J. Vetter, P. Novák, M. R. Wagner, C. Veit, K.-C. Möller, J. O. Besenhard, M. Winter, M. Wohlfahrt-Mehrens, C. Vogler, and A. Hammouche, *J. Power Sources*, **147**, 269 (2005).
- T. Waldmann et al., *J. Electrochem. Soc.*, **163**, A2149 (2016).
- T. Waldmann, B.-I. Hogg, and M. Wohlfahrt-Mehrens, *J. Power Sources*, **384**, 107 (2018).
- J. Fleischer, (01/2017), Challenges of high Quality and high Performance Cell Stacking, Prof. Dr.-Ing. Jürgen Fleischer, Mainz, 2017/01/31. (http://cii-resource.com/cet/AABE-03-17/Presentations/BMGT/Fleischer_Juergen.pdf).
- Danae, (2021-02-15), Editorial: Danae. (<https://gropow.com/blog/battery-technology-rolling-vs-stacking-battery-monday.html>).
- E. J. Mittemeijer, *Fundamentals of Materials Science: The Microstructure-Property Relationship Using Metals as Model Systems* (Springer, Berlin) (2021).
- A. S. Mussa, G. Lindbergh, M. Klett, P. Gudmundson, P. Svens, and R. W. Lindström, *Journal of Energy Storage*, **20**, 213 (2018).
- C. Hafner, T. Bernthaler, V. Knoblauch, and G. Schneider, *Practical Metallography*, **49**, 75 (2012).
- C. Weisenberger, D. K. Harrison, T. Bernthaler, G. Schneider, and V. Knoblauch, *Practical Metallography*, **57**, 176 (2020).
- T. C. Bach, S. F. Schuster, E. Fleder, J. Müller, M. J. Brand, H. Lorrmann, A. Jossen, and G. Sextl, *Journal of Energy Storage*, **5**, 212 (2016).
- V. Yufit, P. Shearing, R. W. Hamilton, P. D. Lee, M. Wu, and N. P. Brandon, *Electrochem. Commun.*, **13**, 608 (2011).
- V. Müller, R. Bernhard, J. Wegener, J. Pfeiffer, S. Rössler, R.-G. Scurtu, M. Memm, M. A. Danzer, and M. Wohlfahrt-Mehrens, *Energy Technol.*, **8**, 2000217 (2020).
- S. Gorse, B. Kugler, T. Samtleben, T. Waldmann, M. Wohlfahrt-Mehrens, G. Schneider, and V. Knoblauch, *Practical Metallography*, **51**, 829 (2014).
- J. Lamb and C. J. Orendorff, *J. Power Sources*, **247**, 189 (2014).
- D. P. Finegan et al., *Nat. Commun.*, **6**, 6924 (2015).
- X. Fleury, M. H. Noh, S. Geniès, P. X. Thivel, C. Lefrou, and Y. Bultel, *Journal of Energy Storage*, **16**, 21 (2018).
- A. Pfrang, A. Kersys, A. Kriston, D. U. Sauer, C. Rahe, S. Käbitz, and E. Figgemeier, *J. Power Sources*, **392**, 168 (2018).
- C. Weisenberger, B. Meir, S. Röhrler, D. K. Harrison, and V. Knoblauch, *Electrochim. Acta*, **379**, 138145 (2021).
- J. Swart and D. Slee, *2008 IEEE Symposium on Product Compliance Engineering (IEEE, Piscataway, NJ)* p. 1 (10/2008).
- P. Berg, M. Spielbauer, M. Tillingner, M. Merkel, M. Schoenfuss, O. Bohlen, and A. Jossen, *Journal of Energy Storage*, **31**, 101499 (2020).
- T. Waldmann, S. Gorse, T. Samtleben, G. Schneider, V. Knoblauch, and M. Wohlfahrt-Mehrens, *J. Electrochem. Soc.*, **161**, A1742 (2014).

42. İ. Üçel, P. Gupta, and P. Gudmundson, *Journal of Energy Storage*, **46**, 103845 (2022).
43. P. Gupta, İ. B. Üçel, P. Gudmundson, and E. Olsson, *Exp. Mech.*, **60**, 847 (2020).
44. A. Schilling, J. Schmitt, F. Dietrich, and K. Dröder, *Energy Technol.*, **4**, 1502 (2016).
45. P. Mohtat, S. Lee, J. B. Siegel, and A. G. Stefanopoulou, *J. Electrochem. Soc.*, **168**, 100520 (2021).
46. C. Hogrefe, T. Waldmann, M. B. Molinero, L. Wildner, P. Axmann, and M. Wohlfahrt-Mehrens, *J. Electrochem. Soc.*, **169**, 50519 (2022).
47. S. A. Channagiri, S. C. Nagpure, S. S. Babu, G. J. Noble, and R. T. Hart, *J. Power Sources*, **243**, 750 (2013).